Chaotic ionization of a highly excited hydrogen atom in parallel electric and magnetic fields

Türker Topçu and Francis Robicheaux

Department of Physics, Auburn University, AL 36849-5311, USA

Abstract
We present results of our simulations of the ionization of a hydrogen atom
excited to a Rydberg wave packet in the presence of external parallel electric
and magnetic fields. This is an example of an open, *quantum* system whose
classical counterpart has been shown to display chaos in the time domain.
Within the framework of classical mechanics, electrons escape through chaos
induced pulse trains. We reproduce such previously observed signatures of
classical chaos in the time-dependent current of ionizing electrons and study
the interference effects between the outgoing pulse trains which is absent in
the classical picture. Our attempts at manipulating the ionization pulse trains
and the effect of core scattering coupled with the chaotic ionization are also
discussed. We further investigate the onset of chaos as a function of the
scaled energy of the system. We find that for relatively high magnetic fields,
quantum-mechanical ionization current shows erratic fluctuations in contrast
with the classical current which shows transition to regularity. We conclude
that the oscillations result from the decrease in the number of the ionization
channels for the higher magnetic field strengths. We further study the time-
dependent autocorrelation function and its Fourier transform to look for the
effects of the Landau quantization in the photoabsorption spectrum. Our results
include calculations via the classical trajectory Monte Carlo method to compare
our non-perturbative quantum-mechanical results with the underlying chaotic
classical dynamics.

(Some figures in this article are in colour only in the electronic version)

1. Introduction

Within the last two decades, systems whose underlying classical mechanics exhibit chaos
have attracted much attention both from the theoretical and the experimental point of view.
Considerable effort has been made to observe and explain chaotic behaviour within the
purely quantum-mechanical framework. These efforts resulted in observations of a rich

variety of signatures of chaos in the energy level statistics [1], wavefunctions [2], absorption–ionization spectra [3–5] etc of quantum systems whose classical counterparts exhibit chaos. Unfortunately, attempts to explain the physical origins of such *irregular* behaviour in quantum mechanics have failed and it was found that even though quantum systems imitate classical systems for a finite time, the classical chaos is suppressed in quantum systems in the long time limit. In the sense of positive Liapunov exponents, chaos does not exist in quantum mechanics, mainly due to the linearity of the Schrödinger equation. Due to its lack of origin in quantum mechanics, much work went into developing semiclassical and statistical quantum-mechanical theories such as random matrix theory [6] to study manifestations of classical chaos in quantum systems [7]. Unbounded irregular scattering has attracted particular attention to generalize certain signatures of chaos to a wide variety of systems since Blümel and Smilansky [8] showed that Ericson fluctuations are a universal phenomenon. These fluctuations were originally proposed by Ericson [9] as a signature of chaos in the photoabsorption spectrum of compound nuclear reactions before their experimental observation [10].

Besides many systems, Rydberg atoms and wave packets have been particularly useful in studying how classically chaotic dynamics is manifested in their quantum-mechanical counterparts. This is because Rydberg atoms provide a real non-separable physical system with just a few degrees of freedom whose classical counterpart exhibits chaos in external magnetic and combinations of magnetic and electric fields. Rydberg atoms in various combinations of static [11–13] fields have also been studied and several useful theoretical and computational tools have been developed during this process [14, 15].

Chaotic ionization of Rydberg systems has been investigated in the energy domain both classically and semiclassically for different regimes of microwave ionization [16] characterized by a scaled frequency. Furthermore, classical theories such as closed orbit theory have been developed to analyse long range chaotic fluctuations in the photoabsorption spectra to interpret spectra of atoms in external fields. But there is a lack of effort in the exploration of chaotic ionization dynamics in the time domain. Recently Mitchell *et al* performed classical calculations to investigate ionization of a hydrogen atom in parallel electric and magnetic fields as an example of chaotic escape dynamics in an open system in the time domain [17, 18]. In their simulations, they excited a hydrogen atom to a Rydberg state with $n \sim 80$ and studied the time-dependent structure of the ionization rate for a distribution of launch angles and energies. They observed distributions of electrons ionizing via a train of pulses—a consequence of the classical chaos induced by the external magnetic field. They looked at the ionization rate and studied the initial launch angular distribution of the classical trajectories as a function of the time it takes the electrons to reach their detector. They observed a self-similar structure in the launch angle versus time distribution which they were able to link to a fractal structure. They showed that each escape segment in the launch angle-time distribution corresponds to a particular pulse in the pulse train of the ionizing electrons and therefore the fractal structure of the launch angle versus time distribution is directly reflected in the time-dependent ionization-rate. They also argued that the true quantum-mechanical treatment of this problem may bring in some interesting effects due to interference and the Heisenberg uncertainty principle. The purpose of this paper is to investigate these purely quantum-mechanical effects and to explore quantum signatures of the underlying classical chaos for this system in the time domain.

In this paper, we discuss results from our non-perturbative quantum-mechanical and classical trajectory Monte Carlo (CTMC) calculations and observe ionization pulse trains induced by chaos. We present results on time-dependent ionization of a hydrogen atom excited to high Rydberg levels around $n = 40, n = 60$ and $n = 80$ by a short laser pulse in parallel electric and magnetic fields. We have further extended our calculations up to $n = 120$ and observed very similar behaviour in the time-dependent dynamics that we have seen for

the lower n values. We look at the current of ionizing electrons as a function of time through a spherical detector placed just outside the peak of the potential. We compare these results with those from our CTMC calculations to see the extent to which the Bohr correspondence principle holds. We look at the wavefunction of the system as a function of time and investigate angular momentum distribution of the escaping electrons as they hit the detector. We compare our results with the classical calculations of Mitchell *et al* [17, 18] where possible. We study the time evolution of the interference patterns on the detector. We observed dependence of the escape time of a trajectory on its classical launch angle which incited us to manipulate the pulse train by placing nodes at certain angles into the angular distribution of the initial wave packet in our quantum wave packet calculations. At this point, we introduce core scattering into the problem via a model core potential and explore the coupling between two different mechanisms that produce ionization pulse trains. Then we turn to the question of the onset of chaos in our system and introduce scaled energy E_c to examine the transition from chaotic ionization dynamics to regularity as we vary the magnetic field strength. We also study the time-dependent autocorrelation function and the corresponding spectral autocorrelation function to look for any effects of Landau quantization, such as the quasi-Landau oscillations. We perform our quantal and classical calculations in parallel in each of these sections to see if the Bohr correspondence principle applies in each case.

2. Theory

In the following two subsections, we discuss methods of non-perturbative quantum-mechanical wave packet and the classical trajectory Monte Carlo (CTMC) calculations. We use atomic units throughout this paper unless we state otherwise.

2.1. The quantum-mechanical time-dependent wave packet method

The total Hamiltonian of a hydrogen atom in parallel electric and magnetic fields is

$$H_0 = -\frac{1}{2}\frac{\mathrm{d}^2}{\mathrm{d}r^2} - \frac{1}{r} + \frac{l(l+1)}{2r^2} + \frac{\gamma}{2}L_z + \frac{\gamma^2}{8}r^2\sin^2\theta + \mathcal{F}r\cos\theta \tag{1}$$

where $\gamma = B/(2.35 \times 10^5 \text{ T})$ is the magnetic field strength in atomic units when B is in T, and $\mathcal{F} = F \times (1.94 \times 10^{-10} \text{ au (V cm)}^{-1})$ is the electric field strength in atomic units when F is in V cm^{-1}. The external fields are taken to be in the z-direction such that $\vec{B} = B\hat{z}$ and $\vec{F} = F\hat{z}$, respectively. A detailed account of the approximations made in the Hamiltonian 1 can be found in [19]. We break up the Hamiltonian H_0 into two pieces: the atomic Hamiltonian H_a and the static field Hamiltonian H_f,

$$H_0 = H_a + H_f, \tag{2}$$

and introduce a laser term H_l to excite the hydrogen atom to a Rydberg state with energy E,

$$H = H_0 + H_l \tag{3}$$

with

$$H_a = -\frac{1}{2}\frac{\mathrm{d}^2}{\mathrm{d}r^2} - \frac{1}{r} + \frac{l(l+1)}{2r^2} \tag{4a}$$

$$H_f = \frac{\gamma}{2}L_z + \frac{\gamma^2}{8}r^2\sin^2\theta + \mathcal{F}r\cos\theta \tag{4b}$$

$$H_l = \zeta(t)\,\mathrm{e}^{-\mathrm{i}(E-E_g)t}r\cos\theta \tag{4c}$$

where $\zeta(t) = \exp\left\{-t^2/t_w^2\right\}$ is the Gaussian laser pulse and E_g is the energy of the initial ground state that is being excited. We use first-order time-dependent perturbation theory to evaluate the time-dependent wavefunction of the system. The total first-order wavefunction $\Psi(\vec{r}, t)$ within the time-dependent perturbation theory is

$$\Psi(\vec{r}, t) = \psi(\vec{r}, t)\, e^{-iEt} + \psi_g(\vec{r})\, e^{-iE_g t}. \tag{5}$$

Here $\psi_g(\vec{r})$ is the wavefunction of the initial ground state that is being excited to the Rydberg state with energy E. $\psi(\vec{r}, t)$ is the wave packet excited by the laser. Within this approximation, the time-dependent Schrödinger equation for $\psi(\vec{r}, t)$ reads [20]

$$\left(i\frac{\partial}{\partial t} - (H_0 - E)\right)\psi(\vec{r}, t) = S_0(r, t). \tag{6}$$

Note that the energy E of the Rydberg state that is being excited is subtracted from the diagonal elements of the Hamiltonian to reduce the numerical errors due to phase accumulation. We choose the source term $S_0(r, t)$ to be spherically symmetric and spatially compact. It is launched to a Rydberg state with energy E by a short laser pulse:

$$S_0(r, t) = \delta_{l,0}\, \zeta(t)\, r^2\, e^{-r/2}. \tag{7}$$

The laser pulse peaks at $t = 0$ and we start time propagating equation (6) at $t = -6t_w$ where t_w is the width of the laser pulse. In our calculations, we have chosen t_w to be $\tau_{Ryd}/15$ where $\tau_{Ryd} = 2\pi(-2E)^{-3/2}$ is the Rydberg period of the state being excited. Integrating equation (6) over one time step and using the trapezoidal rule for the integrations, one obtains

$$i[\psi(t + \delta t) - \psi(t)] = \frac{\delta t}{2}((H_0 - E)[\psi(t + \delta t) + \psi(t)] + [S_0(t + \delta t) + S_0(t)]) \tag{8}$$

which yields the quantum propagator,

$$\psi(t + \delta t) = \left(\frac{1 - i(H_0 - E)\delta t/2}{1 + i(H_0 - E)\delta t/2}\right)\psi(t) - \frac{i\delta t}{1 + i(H_0 - E)\delta t/2}S_0\left(t + \frac{\delta t}{2}\right) + \mathcal{O}[\delta t^3]. \tag{9}$$

We further make the approximation

$$\frac{i\delta t}{1 + i(H_0 - E)\delta t/2} \simeq i\delta t + \frac{\delta t^2}{2}(H_0 - E) + \mathcal{O}[\delta t^3] \tag{10}$$

for the second term on the right-hand side which preserves the order of the propagator. The operator acting on $\psi(t)$ in equation (9) is the lowest order Padé approximation to the time evolution operator $e^{-iH_0 t}$. We therefore evaluated the first term on the right-hand side of equation (9) by means of the split operator technique without altering the order of the propagator. We used a higher order split operator technique than that employed in [22, p 2]. We have found that going to higher order in the split operator technique significantly reduced the phase errors.

$$\psi(t + \delta t) = \left(\frac{1 - iH_f\delta t/4}{1 + iH_f\delta t/4}\right)\left[\left(\frac{1 - i(H_a - E)\delta t/4}{1 + i(H_a - E)\delta t/4}\right)\left[\left(\frac{1 - i(H_a - E)\delta t/4}{1 + i(H_a - E)\delta t/4}\right)\right.\right.$$
$$\times \left[\left(\frac{1 - iH_f\delta t/4}{1 + iH_f\delta t/4}\right)\psi(t) - \frac{1}{4}\left(i\delta t + \frac{\delta t^2}{2}(H_0 - E)\right)S_0\left(t + \frac{\delta t}{2}\right)\right]$$
$$\left.-\frac{1}{2}\left(i\delta t + \frac{\delta t^2}{2}(H_0 - E)\right)S_0\left(t + \frac{\delta t}{2}\right)\right] - \frac{1}{4}\left(i\delta t + \frac{\delta t^2}{2}(H_0 - E)\right)S_0\left(t + \frac{\delta t}{2}\right)\right]$$
$$+ \mathcal{O}[\delta t^3]. \tag{11}$$

The effect of the external fields on the solutions of the field free hydrogen atom can simply be deduced by noting that (see [21, p 250])

$$\cos\theta\, Y_l^m = \sqrt{\frac{(l+1)^2 - m^2}{(2l+1)(2l+3)}}\, Y_{l+1}^m + \sqrt{\frac{l^2 - m^2}{(2l+1)(2l-1)}}\, Y_{l-1}^m \tag{12}$$

$$\sin^2\theta\, Y_l^m = -\sqrt{\frac{[(l+1)^2 - m^2][(l+2)^2 - m^2]}{(2l+1)(2l+3)^2(2l+5)}}\, Y_{l+2}^m$$

$$+ \left[1 - \frac{(l+1)^2 - m^2}{(2l+1)(2l+3)} - \frac{l^2 - m^2}{(2l+1)(2l-1)}\right] Y_l^m$$

$$- \sqrt{\frac{[l^2 - m^2][(l-1)^2 - m^2]}{(2l+1)(2l-1)^2(2l-3)}}\, Y_{l-2}^m. \tag{13}$$

From this it can be seen that the electric field mixes state l with states $l \pm 1$ and the magnetic field mixes state l with states $l, l \pm 2$. A natural representation of the wavefunction can be realized on an (l, r) grid. On this grid, operator H_f acts only along the l-direction and it is pentadiagonal. The atomic Hamiltonian H_a acts along the r-direction and involves the usual kinetic energy operator and the Coulomb potential. We describe the second derivative in the kinetic energy within the three-point differencing scheme and therefore H_a is tridiagonal in r (see [22]) and diagonal in l. The number of points N_l in the l-direction are chosen to be 150, 200 and 250 for $n = 40, n = 60$ and $n = 80$ cases, respectively. The number of points N_r in the r-direction are 1000, 1500 and 2500 for $n = 40, n = 60$ and $n = 80$ and the results we present are converged with respect to N_l and N_r.

We use square root mesh along the r-direction of the grid as described in [22]. The radial extent of the spatial direction on the grid, i.e., box size r_f, is chosen to be twice the radial extent of the peak of the potential, i.e., $r_f \sim 2r_p$. The number of points in this direction is chosen such that the maximum r-mesh spacing δr_{max} is less than $0.5/p_{max}$ where p_{max} is the largest possible linear momentum an ionized electron can attain, i.e.,

$$p_{max} = \sqrt{-2(E - V(r_f))} = \sqrt{(1/n^2) + 5\sqrt{F}}. \tag{14}$$

The time step we use for the time propagation of equation (9) is chosen such that it is smaller than the time scales involved in our problem. The time scale set by the electric field can be deduced from the electric field part of the propagator in equation (11);

$$\exp\{-izF\delta t/2\} \simeq \frac{1 - izF\delta t/4}{1 + izF\delta t/4} \tag{15}$$

which is $\sim -i$ for $zF\delta t/4 \sim 1$, giving a $\pi/2$ phase shift. This constricts the appropriate time step below $4/(Fr_f)$. In the same manner, the magnetic field part of the propagator contributes another $\pi/2$ phase error when $\exp\{-iB^2\rho^2\delta t/16\} \sim 1$ which implies $\delta t \lesssim 32/(B^2 r_f^2)$. The time step is also chosen to be much less than the Rydberg period of the state corresponding to the energy E, specifically, $\delta t \sim \tau_{Ryd}/800$. We have performed convergence checks with respect to both δr_{max} and δt and the results we present are converged within a per cent.

Since we are using a finite size box to time propagate the wavefunction, we use a mask function to absorb current that reaches the end of the box to prevent reflections from the box edge. The form of the mask function is $M(r) = 1 - s\,\delta t((r - r_m)/(r_f - r_m))^2$ and it spans the radial range from $r_m = (1/\sqrt{F} + 2r_f)/3$ to r_f. The parameter s quantifies the strength of the absorption. To remove the part of the wavefunction that reaches the end of the box, we

simply multiply the wavefunction with $M(r)$ for each l on the grid after each time step during the time propagation.

Since we are interested in time-dependent current of ionizing electrons, we calculate the probability current density through a spherical detector which we then integrate over the surface to obtain the current as a function of time. We place the detector such that its surface is located just outside the peak of the potential. When the electron goes beyond this peak in space it is considered ionized. Since the peak of the potential is located at $r_p = 1/\sqrt{F}$, we chose the radius of our spherical detector at $r_s = (r_p + 2r_f)/3$. The total current through the surface of the detector is therefore

$$\Phi = -\mathrm{Re}\left[\mathrm{i} \sum_l \psi^*(r_s, l, t) \frac{\partial \psi_l(r, l, t)}{\partial r}\bigg|_{r=r_s} \right]. \tag{16}$$

To check our codes, we have also calculated the total current as the rate of change of the total probability that lies within the spherical region enclosed by the detector after the laser pulse is turned off. We find total agreement between the two methods as expected since

$$\frac{\partial \wp(r, t)}{\partial t}\bigg|_{r=r_s} = -\frac{\partial j(r, t)}{\partial r}\bigg|_{r=r_s} \tag{17}$$

where $\wp$ is the survival probability density within the spherical region and j is the probability current density through the surface of the detector.

2.2. The classical trajectory Monte Carlo method

To compare results of the fully quantal time-dependent formalism to the underlying classical dynamics, we have also performed classical calculations in the framework of the classical trajectory Monte Carlo (CTMC) method. We solved Newton's equations for the trajectory of the hydrogenic electron in the presence of the external parallel electric and magnetic fields using fourth-order adaptive time step Runga–Kutta algorithm described in [23]. We worked in Cartesian coordinates and time propagated the trajectories until certain criteria are met. Time propagation of a trajectory is terminated when the electron passes through the spherical detector or when a predefined final propagation time t_f is reached. When the propagation of Newton's equations is terminated, it is binned in time as an escaped trajectory or discarded depending on whether the electron has reached at the detector or not. After a large number of trajectories are calculated, what is left is a probability distribution of survival in time within the spherical region inside the detector. Each bin in time contains a fraction of probability to escape within the corresponding time interval. Integrating this probability distribution over time up to a particular bin τ gives the probability of survival $P(\tau)$ inside the spherical region up until the time τ. Widths of the time bins in our calculation are $d\tau = t_f/200$. From this survival probability, current through the spherical detector is evaluated as $(P(\tau) - P(\tau - d\tau))/d\tau$. To have good statistics, we had to sample a large number of trajectories and we have checked convergence with respect to the number of trajectories to insure good statistics. The results we present here have been obtained with 3×10^6 classical trajectories.

To closely match the fully quantal case, each classical trajectory is launched in a spherically symmetric fashion, i.e., the distribution of the cosine of the angle θ at which a trajectory is launched is chosen from a flat distribution to mimic the angular distribution of the initial quantum wave packet. The azimuthal angle φ is a cyclic coordinate due to the cylindrical symmetry of the problem. There are three random initial parameters for each launched trajectory in our calculations: the cosine of the launch angle of the trajectory, launch time distribution $\mathcal{F}(t)$, and initial energy distribution $\mathcal{G}(\epsilon)$ of the trajectory. The launch
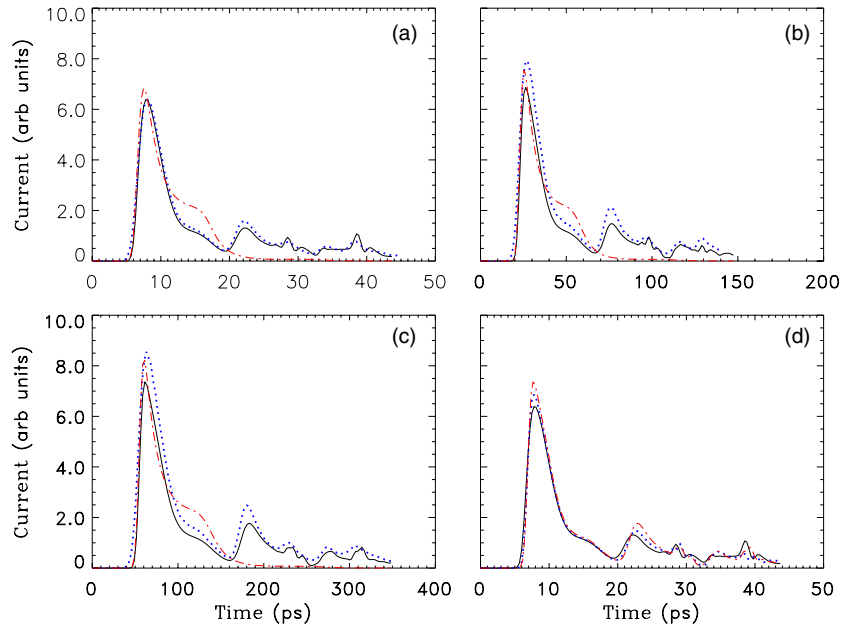
Figure 1. Current–time plots for ionization with excitation to (a) $n = 40$, (b) $n = 60$ and (c) $n = 80$ states of hydrogen via a short laser pulse in parallel electric and magnetic fields. Results from quantum-mechanical wave packet (black solid curve) and CTMC (blue dotted curve) calculations are plotted on top of each other along with the pure electric field case (red dash-dotted curve). Part (d) shows just the quantum-mechanical current–time plots in (a)–(c) plotted together for comparison. (Colour online.)

time distribution is given by the squared absolute value of the Gaussian laser pulse $\zeta(t)$ in equation (4), and the energy distribution $\mathcal{G}(\epsilon)$ is evaluated as the squared absolute value of the Fourier transform of $\zeta(t)$:

$$\mathcal{F}(t) = e^{-2t^2/t_w^2} \qquad \mathcal{G}(\epsilon) = e^{-(\epsilon-E)^2 t_w^2/2}. \tag{18}$$

Here E is the central energy of the laser pulse, and t_w is the width of the laser pulse in time. We have generated these Gaussian distributions of launch time and initial energy using the methods described in [23]. The laser pulse used to excite the Rydberg states is exactly the same as that used for the quantum wave packet calculations.

3. Results

3.1. Flux of ionizing electrons

Results from the calculations for the current of ionizing electrons through the spherical detector for $n = 40, 60$ and 80 can be seen in figures 1(a)–(c) respectively. Figures show both quantum-mechanical (black solid curve) and classical (blue dotted curve) calculations to contrast the quantum-mechanical current with its classical counterpart which exhibits chaos. The electric and magnetic field strengths for the $n = 40$ calculations are $B = 3.92$ T and $F = 304$ V cm^{-1}. For the cases of $n = 60$ and 80, we scaled the magnetic field we used for $n = 40$ by $1/n^3$ and the electric field by $1/n^4$ to stay at the same dynamical regime. The external field strengths for these calculations are chosen such that the system is in the n-mixing regime and the energy is

above the classical ionization threshold. The box sizes used in each of the quantum-mechanical calculations are 8000, 18 000, and 32 000 (au) for $n = 40$, $n = 60$ and $n = 80$ respectively and the width of the laser pulse is $t_w = \tau_{Ryd}/15$. As pointed out in [18], the actual resolution of the pulses in the pulse train is determined by the interplay of Δt and ΔE. Therefore, since both Δt and ΔE contribute to the broadening of the pulses, there exists an optimal set of $(\Delta t, \Delta E)$ for which the ionization pulses along the time axis are the sharpest. We have found that a longer pulse duration than we defined above actually gives a noticeably sharper pulse train than that seen in figure 1. The number of angular momenta included in each calculation scales roughly as $\sim n$ and is 150 for $n = 40$. We time propagate the wavefunction ψ for $(9/2)\tau_{Ryd}$ in each case of n. We have also extended our calculations up to $n = 120$ and did not find any significant shifts from the time-dependent dynamics we describe below for lower n values.

Whether a classical electron will ionize or not, and the time of its ionization, depend on the initial launch angle θ of the classical trajectory. The trajectories that are launched directly downhill, i.e., at $\theta = \pi$, will be the first ones to ionize. Ionization current due to these electrons makes up the first prominent pulse in each of the figures in figure 1, which is called the direct pulse. Classically, this corresponds to the first prominent escape segment in the self-similar pattern of the classical launch angles versus time seen in figures 2(a) and (b) of [18].

A remake of figures 2(a) and (b) of [18] can be seen in figure 2, which is generated using the data kindly supplied to us by K A Mitchell. Figure 2(a) shows two time-dependent ionization rate curves as a function of scaled time t, which is related to the real physical time $\hat{t}$ through $t = \hat{t}n^3$. The calculation is for $n = 80$ in parallel electric and magnetic fields of $F = 19$ V cm^{-1} and $B = 0.49$ T. The ionization rate depicted by the black solid line is calculated using an ensemble of trajectories with a precise energy and launch time, whereas the smooth red solid line is calculated using a Gaussian wave packet (see [18] for more detail). Figure 2(b) shows the time it takes for a trajectory to ionize as a function of its launch angle. This launch angle distribution is referred to as the escape-time plot in [18]. Each of the *icicles* in this plot marks out a range of launch angles such that when a trajectory is launched at an angle from within this range, it ionizes through a particular pulse in figure 2(a). These icicles are called escape segments and every escape segment gives rise to a particular pulse in the ionization rate. The dotted lines in figure 2(b) match each escape segment with its corresponding pulse in the ionization pulse train. The escape segments of figure 2(b) show a self-similar structure and [18] connects this structure to fractal structure in the classical mechanics of the escape dynamics.

In the self-similar pattern of launch angles seen in figure 2(b), the trajectories launched from within the angular range $2.23 < \theta < \pi$ rad make up the direct ionization pulse. This escape segment is by far the widest compared to the rest of the escape segments in the pattern. Also note that all the direct pulses seen in figure 1 terminate with a *knee* structure. This knee is due to the electrons that were not launched directly downhill but at a slightly smaller or larger angle. They are turned around by the force from the electric field before they can scatter from the nucleus and reach the detector before the direct pulse of electrons has completely passed through the detector. This knee is absent in the previous classical calculations of Mitchell *et al* where they used a minimum uncertainty Gaussian wave packet for their ensemble of trajectories to obtain a smooth ionization rate curve, as that seen in figure 2(a). In some of their calculations [17], the direct pulse is smaller than the second peak in the pulse train whereas our calculations and the calculations presented in figure 2(a) yield a larger prominent direct pulse compared to the rest of the peaks in the pulse train. This is due to the fact that [17] uses a p_x angular distribution for the initial launch angles of the trajectories while
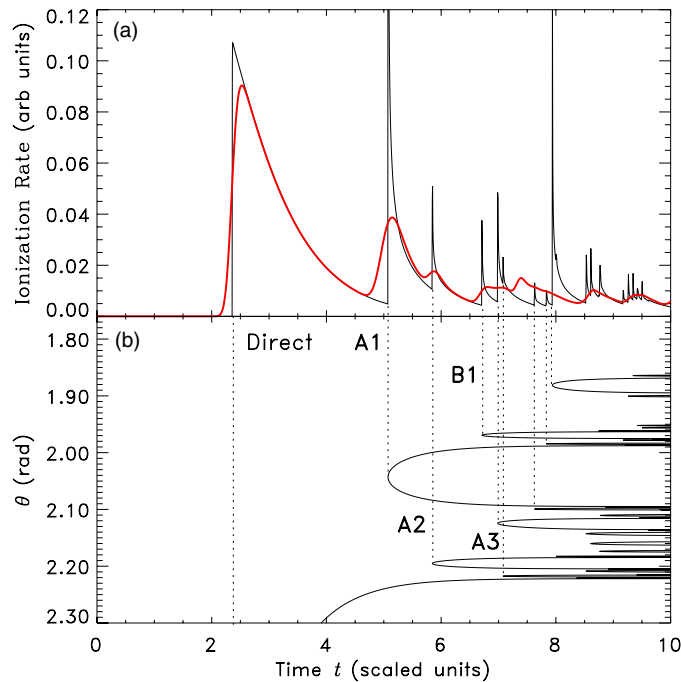
Figure 2. Classical calculations of [18] for the ionization of hydrogen in parallel electric and magnetic fields of $F = 19$ V cm^{-1} and $B = 0.49$ T for $n = 80$. Part (a) shows the ionization rate as a function of scaled time, and part (b) shows the scaled time for a trajectory to escape as a function of its launch angle. The black solid curve in (a) is calculated using an ensemble of trajectories with a precise launch time and energy whereas the smooth red solid curve is calculated using a Gaussian distribution for the energy and the launch time. Each of the escape segments seen in (b) corresponds to a particular pulse in the ionization rate and is matched with their pulse via the dotted lines. The escape segment that gives rise to the direct pulse peaks at $\theta = \pi$ and most of it falls outside the θ range plotted. (We thank K A Mitchell for kindly supplying the data for this partial replot of figure 2 of [18]. We also thank K A Mitchell and J B Delos for their permission to include this replot in this paper.)

figure 2 and we use an s-wave distribution. Irregular peaks that come after the direct pulse in the pulse train are the electrons that were launched from angles outside of $\theta \sim \pi \pm 0.94$ rad. Their ionization is delayed for different durations of time depending on their launch angle. The trajectories perform a cyclotron motion due to the magnetic field while going down the potential hill as seen from the wavefunction plots of figure 3. Classically, these trajectories originate from the various smaller escape segments marked as **A1**, **A2**, **A3**, etc in figure 2(b). As the pulse train grows longer, more escape segments contribute to a given pulse in the pulse train. Therefore one would expect that these later pulses in the pulse train would show quantum-mechanical interference effects most prominently. This is indeed displayed in the time-dependent wavefunctions seen in figure 3. The fact that the launch angle of a classical trajectory determines its place in the pulse train suggests that by manipulating the launch angle distribution of the trajectories, we can tailor the pulse train to a desired shape (see section 3.4).

Figure 3 shows snapshots of the probability distribution $|\psi|^2$ in time for $n = 80$ in the ρ–z plane. The nucleus is positioned at the origin and the force from electric field is pointing in
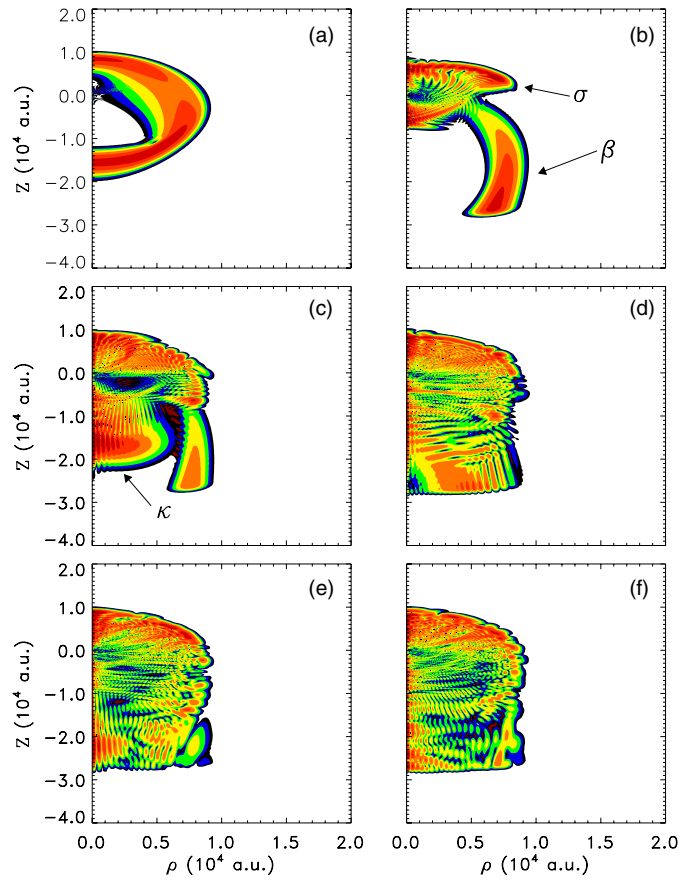
Figure 3. Snapshots of the absolute value squared wavefunction of hydrogen in parallel electric and magnetic fields for the $n = 80$ case at (a) 58 ps, (b) 117 ps, (c) 175 ps, (d) 233 ps, (e) 292 ps and (f) 350 ps. In (b), σ marks the part of the wavefunction that shows Stark oscillation whereas β shows the one that gives rise to the direct ionization pulse in figure 1(c). In (c), κ shows the part of the wavefunction that is responsible for the second peak in the pulse train.

the negative z-direction. At $t = 58$ ps (figure 3(a)), the spherically symmetric outgoing wave is seen just when the current is near the peak of the direct pulse in figure 1(c). This outgoing wave gives rise to the direct ionization pulse. At $t = 117$ ps (figure 3(b)), the first pulse of ionizing electrons reaches the spherical detector and gets absorbed by the spherical mask just after it crosses the detector surface at $r = 2.68 \times 10^4$ (au). The part of the wavefunction that corresponds to the ionizing electron current density (labelled as β in figure 3(b)) goes downhill as it performs a cyclotron motion due to the magnetic field parallel to the electric field. This β part of the wavefunction is the direct pulse of figure 1(c), at the time when the current reaches the knee of the direct pulse along the pulse train. Note that this part of the wavefunction does not yet show any interference patterns. This is due to the fact that it corresponds to the classical trajectories launched from within the first prominent escape segment in figure 2(b). The part of this escape segment that makes up the direct pulse has no angular overlap with the rest of the escape segments. This means that there is only one way for a trajectory to escape during the direct pulse and that is to be launched from within this first escape segment. The lack of

alternative escape paths results in no interference patterns in the wavefunction. The part of the wavefunction marked by σ is relatively localized between $0 < z < 1 \times 10^4$ (au) and shows the Stark oscillating part of the wavefunction. Nodes of this part of the wavefunction corresponds to the nodes of the Stark sublevels. Figure 3(c) shows the wavefunction at $t = 175$ ps, near the peak of the second pulse in figure 1(c). The wavefunction shows two types of scattering: the β part seen in figure 3(b) and a part that is going directly down the potential hill (marked as κ). The β part makes up the skirt of the direct pulse in figure 1(c) onto which the second pulse sits. The κ part of the wavefunction gives rise to the second pulse in the pulse train. Note that there is an interference pattern on this part of the wavefunction which is due to the interference between the components of the wavefunction moving in the opposite direction along the ρ dimension as they perform cyclotron motion rolling down the potential hill. The classical escape segment responsible for the second pulse has an angular overlap with the first prominent escape segment of figure 2(b), which is causing interference between the κ and the β parts of the wavefunction. Figure 3(d) shows the wavefunction at $t = 233$ ps, around the third pulse in figure 1(c). The β and the κ parts of the wavefunction has now completely blended into each other such that the β part of the wavefunction is hardly recognizable. This is so since the escape segment that gives rise to the third pulse in figure 2(b) now overlaps in angle with both the first prominent escape segment as well as the escape segment **A1** which is responsible for the second pulse. The increased number of ways to escape during the third pulse results in interference between these channels, leading to interference between the β and the κ parts of the wavefunction. The interference patterns formed show two standing wave patterns perpendicular to each other with roughly the same wavelength suggesting that both components have similar momentum. Figures 3(e) and (f) sample the wavefunction further along the pulse train $t = 292$ ps and $t = 350$ ps. In these cases, the interference patterns in the wavefunction are noticeably more complicated than those of the earlier times. The classical escape segments corresponding to these later times overlap with all the escape segments that gave rise to the previous pulses, resulting in the ever increasing complexity of the interference patterns. The interference patterns are dynamic, and resemble scars of the classical periodic orbits going downhill as they perform a cyclotron motion about the z-axis. Such scars are commonly observed in bound-state eigenfunctions of classically chaotic Hamiltonian systems [2] and are well-known signatures of chaos in quantum systems.

The classical chaotic dynamics of this open system can be attributed to the presence of the external magnetic field, without which the dynamics would be regular. To check this, we have extended our quantum-mechanical wave packet calculations to exclude the magnetic field. This should result in a single prominent pulse of ionization in the absence of core electrons, and this is indeed in accord with our results (red dash-dot-dash curves in figures 1(a)–(c)).

Figure 1(d) shows all three quantum-mechanical calculations for $n = 40$, 60 and 80 on top of each other to see if there is any effect due to the $1/n^3$ decreasing of the Rydberg level spacings as n is increased. We see no significant differences within the n range we investigate.

3.2. l-distributions of ionizing electrons

Figure 4 shows the snapshots of the time-dependent angular momentum distribution of $|\psi|^2$ within the region bounded by the spherical detector for $n = 80$. The main plot in each panel is for the case of the parallel electric and magnetic fields whereas the insets are for the pure electric field case. Figures 4(a)–(c) are snapshots of the l-distribution during the direct ionization pulse of figure 1(c) at $t = 44$ ps, $t = 58$ ps and $t = 85$ ps, respectively. The angular momenta of the initially s-wave electrons spread to higher l as the wavefunction expands outward
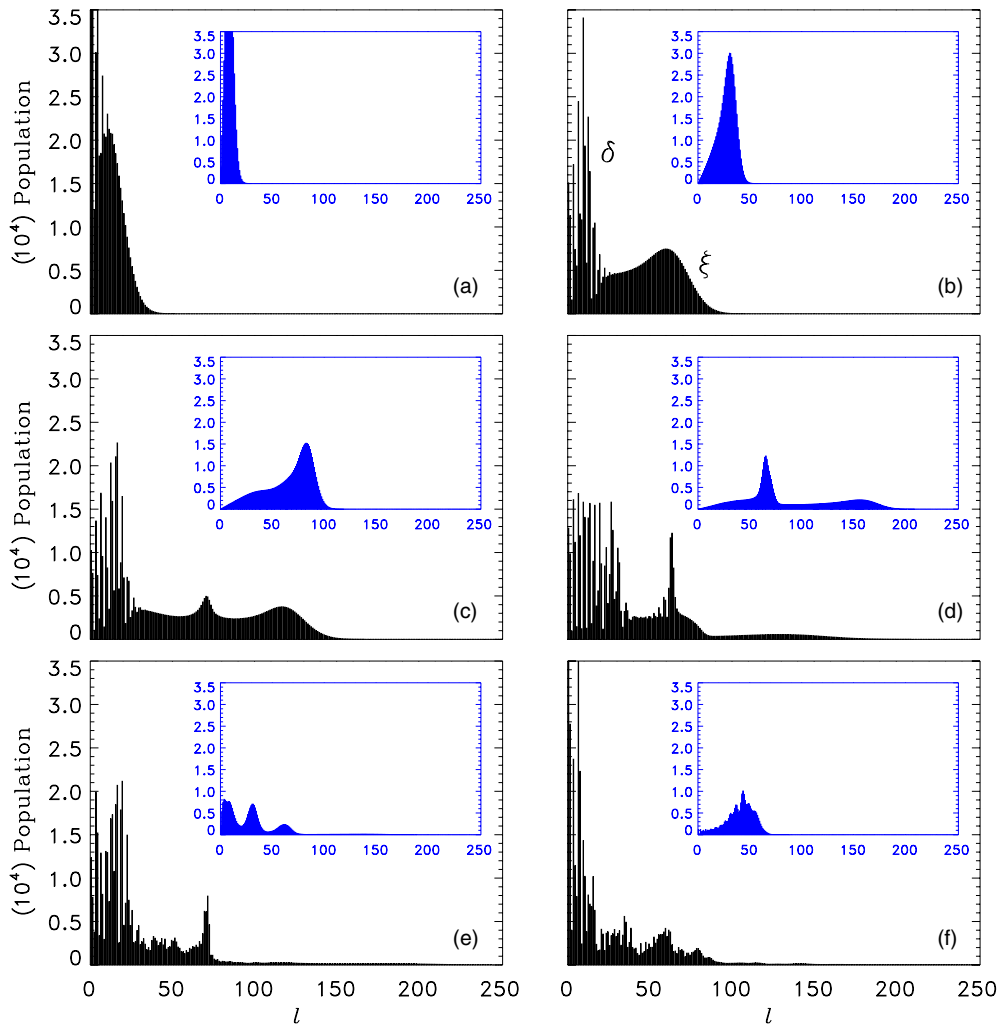
Figure 4. Time evolution of the angular momentum distribution of the electrons within the space bounded by the spherical detector at (a) 44 ps, (b) 58 ps, (c) 85 ps, (d) 129 ps, (e) 234 ps and (f) 338 ps for $n = 80$. The insets show the angular momentum distributions of the electrons at corresponding times for the pure electric field case for which the time-dependent dynamics is regular.

(figure 3(a)). At $t = 58$ ps, the l-distribution shows two distinct types of behaviour: the part of the distribution that propagates out to higher l in the same manner as the pure electric field case (marked as ξ), and the irregular part that remains at low l (marked as δ). Given the fact that the ξ part of the distribution almost coincides with that of the pure electric field case, and in the pure electric field case one ends up with a single prominent ionization pulse, we can conclude that the ξ part of the distribution represents the electrons that are escaping through the direct pulse of figure 1(c). The δ part of the distribution however classically represents the electrons that stay bound in the atom and escape at a later time through another pulse in figure 1(c). The extent of the ξ part of the distribution reaches $l \sim 150$ at $t = 85$ ps. By

this time the direct pulse has well passed its peak and $\sim$13% of the electrons have escaped. Figure 4(d) shows the l-distribution at $t = 129$ ps, just before the knee of the direct pulse reaches the detector. Note that the ξ part of the distribution has almost entirely diminished, leaving behind the δ part from which the second peak in figure 1(c) is about to emerge. Figures 4(e) and (f) are at $t = 234$ ps and $t = 338$ ps, are the snapshots of the l-distribution further along the chaos induced pulse train in figure 1(c). Note that these electrons do not go up as high in l as the population that ionized through the direct pulse.

The distribution starting from small l propagates into larger l's and a small part of it reflects back from $l \sim 200$ and moves back to the smaller l. This oscillation of l between the small and the large angular momenta continues until after the second pulse and the entire population more or less localizes to $l \lesssim 100$. Also note that in the pure electric field case, the irregular features of the l-distribution are absent and the ionization is regular.

3.3. Angular distribution of the ionizing pulse trains on the detector

Figure 1 shows very good agreement between our classical and quantum-mechanical calculations. Note that they show the current that reaches the detector integrated over the surface of the spherical detector. A more detailed look at the distributions of the electrons at the detector surface reveals differences between the classical and quantal pulse trains. Figure 5 shows the time evolution of $|\psi|^2$ on the surface of the spherical detector as a function of θ. The angle θ spans the range $[\pi - \pi/6, \pi + \pi/6]$ for better visualization of the current through the spherical cap. The figure is for $n = 80$ and shows results obtained by both quantum mechanically (black solid curves) and classically (blue dotted curves). Figure 5(a) shows the angular distribution on the detector at $t = 85$ ps, just when the electrons are escaping through the direct pulse in figure 1(c). Note that all the probability density is localized around $\theta = \pi$ since these are the electrons that were originally launched directly downhill. Figures 5(b) and (c) show the angular distribution on the detector at $t = 107$ ps and $t = 151$ ps, at the beginning and the end of the knee of the direct pulse. In figure 5(b), there are no electrons at $\theta = \pi$ and all of the wavefunction hits the detector at $\sim \pi \pm 0.2$ rad, forming a ring that is centred at the point where the z-axis goes through the spherical detector. In figure 5(c), the two peaks in (b) come together at $\theta = \pi$. The quantum-mechanical peaks interfere whereas the classical peaks simply rejoin without interference. The fact that the peaks in figure 5(b) come together is a manifestation of the cyclotron motion the electrons perform as they approach the detector. In figure 5(d) is at $t = 173$ ps, during the second peak in the pulse train. Note that again the wavefunction arrives at the detector in two peaks as in (b), but this time quantum-mechanical peaks show interference even though the peaks are separated. The classical distribution in this case is sharper than that of figure 5(b) meaning that the trajectories that give rise to the second pulse have a sharper distribution of launch angles.

Finally, figures 5(e) and (f) show the angular distribution on the detector at $t = 289$ ps and $t = 347$ ps. These are the distributions of electrons on the detector that escape after the second pulse. Note the interference patterns of the quantum-mechanical distributions are much more complicated and intricate than those of the direct and the second pulses. This points out that the quantum-mechanical distribution shows more and more interference as the pulse train grows longer which is in agreement with our discussions regarding the time-dependent wavefunction in section 3.1. Even though the quantum-mechanical and the classical distributions depicted in figure 5 show fine structural differences due to quantum interference, the effect of the interference in the total current through the sphere is washed out when the current density is integrated over the surface of the detector. This results in the very well agreeing classical and quantum-mechanical time-dependent currents seen in figure 1.
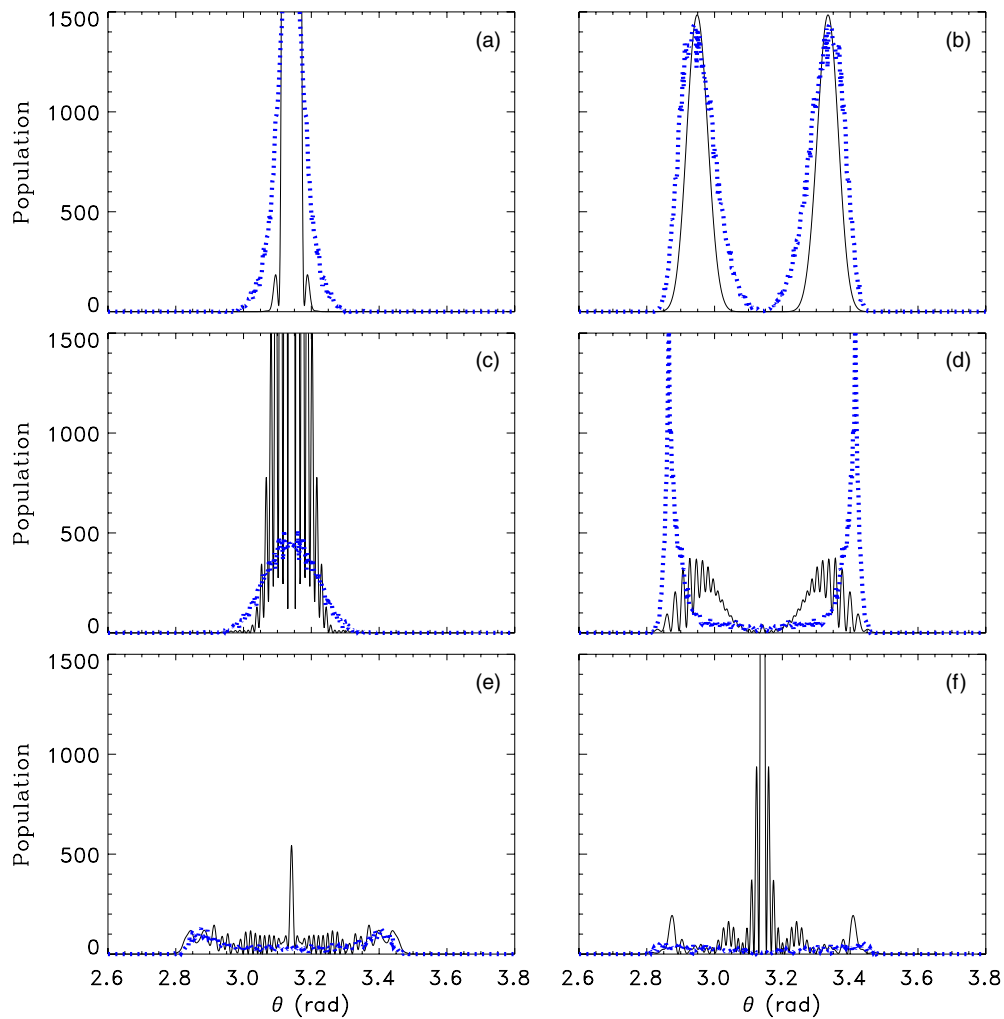
Figure 5. Time evolution of the classical (blue dots) and quantum (black solid line) angular distributions of the electrons hitting the detector at (a) 85 ps, (b) 107 ps, (c) 151 ps, (d) 173 ps, (e) 289 ps and (f) 347 ps for $n = 80$.

3.4. Effect of the angular distribution of the source term

In the quantum-mechanical calculations, we have presented so far, the initial electron wave packet has been chosen to be spherically symmetric. Furthermore, the CTMC results have also assumed a flat distribution of the launch angle of the trajectories. This allowed us to include all the possible trajectories that can be launched in our simulations. As discussed in section 3.1, previous classical calculations [18] and figure 2 suggest that the angle at which a trajectory is launched ultimately defines its time of escape. Therefore, the launch-angular distribution of the trajectories in the classical calculations, or the angular distribution of the initial wave packet in our quantum-mechanical calculations determine the shape of the ionization pulse train.

In this section, we explore the effect of the angular distribution of the initial wave packet in the quantum-mechanical calculations on the structure of the ionization pulse trains. In the classical case, the launch angle distribution of the trajectories determine the relative heights of the peaks in the pulse train which means that the angle at which a trajectory is launched is directly related to its ionization dynamics. For example, the electrons launched from $\theta = \pi$ would be expected to ionize via the direct pulse whereas an electron launched initially uphill, i.e. $\theta < \pi/2$, would escape at a relatively later time via one of the later pulses in the pulse train. This suggests that eliminating certain trajectories from the CTMC calculations that give rise to ionization through a certain pulse in the pulse train may give us the ability to manipulate the structure of the pulse train. This can be realized classically by finding the angular range which spawns the trajectories that escape via a given pulse and excluding these angles from the classical launch angle distribution. In our quantum-mechanical calculations, this would correspond to placing a node in the angular distribution of the initial wave packet.

We have particularly attempted to eliminate the second pulse in figure 1(c) for $n = 80$. To eliminate this second pulse, we needed to know classically at what angle a trajectory must be launched to contribute to this pulse in the train. This was done by binning the trajectories that reached the detector between 158 ps and 213 ps in angle. The result is seen in figure 6(d) as a function of the classical launch angle. The angular range from which a trajectory must originate to contribute to the second pulse is a fairly sharp distribution with a smaller secondary peak. The main peak is centred at $\theta \sim 2.0$ rad whereas the secondary peak is located at $\theta \sim 2.2$ rad. Comparing with figure 2, we realize that these peaks correspond to the escape segments **A1** and **A2** in the escape-time plot, which are responsible for the second and the third peaks in the classical calculations of Mitchell *et al*. Restricting the launch angles of the classical trajectories to outside of this range in the CTMC calculations should therefore eliminate the second peak in the pulse train. The same should also be true in our quantum-mechanical calculations if we place a node at the peak of the angular distribution of figure 6(d) in the angular distribution of the initial wave packet.

Placing a node in the angular distribution of the source term in our quantum-mechanical calculations physically corresponds to superposing a p-wave onto our otherwise s-wave initial wave packet or source term. The radial part of the zero-energy solution to the Schrödinger equation for the hydrogen atom is [24]

$$R_{\infty,l}(r) = \frac{A}{\sqrt{2r}} J_{2l+1}(\sqrt{8r}) \tag{19}$$

where J_{2l+1} is the Bessel function of order $2l+1$, and A is a normalization constant. Therefore, to introduce a node in the wave packet, we superpose a p-wave source $S_1 = \delta_{l,1} r (1-r/2) e^{-r/2}$ with an s-wave source S_0 (see equation (7)) via a mixing coefficient a:

$$\left(\int_0^\infty S_0 J_1(r) \, dr \right) J_1(r) Y_0^0 + a \left(\int_0^\infty S_1 J_3(r) \, dr \right) J_3(r) Y_1^0 = 0. \tag{20}$$

The zero of this superposition for a given angle θ_0 in Y_1^0 yields the mixing coefficient a. The integrals in equation (20) can be evaluated by standard techniques to give an exact result. For the Bessel functions $J_1(r)$ and $J_3(r)$ outside the integrals we have used the asymptotic form of the Bessel function retaining only its outgoing wave part, i.e.,

$$J_m(z) \sim \sqrt{\frac{2}{\pi z}} e^{-i(z - m\pi/2 - \pi/4)}, \qquad (z \gg |m^2 - 1/4|). \tag{21}$$

Solving equation (20) for a, we have found that the mixing coefficient for which there is a single node at $\theta = \theta_0$ is $a = -1.47/\cos(\theta_0)$.
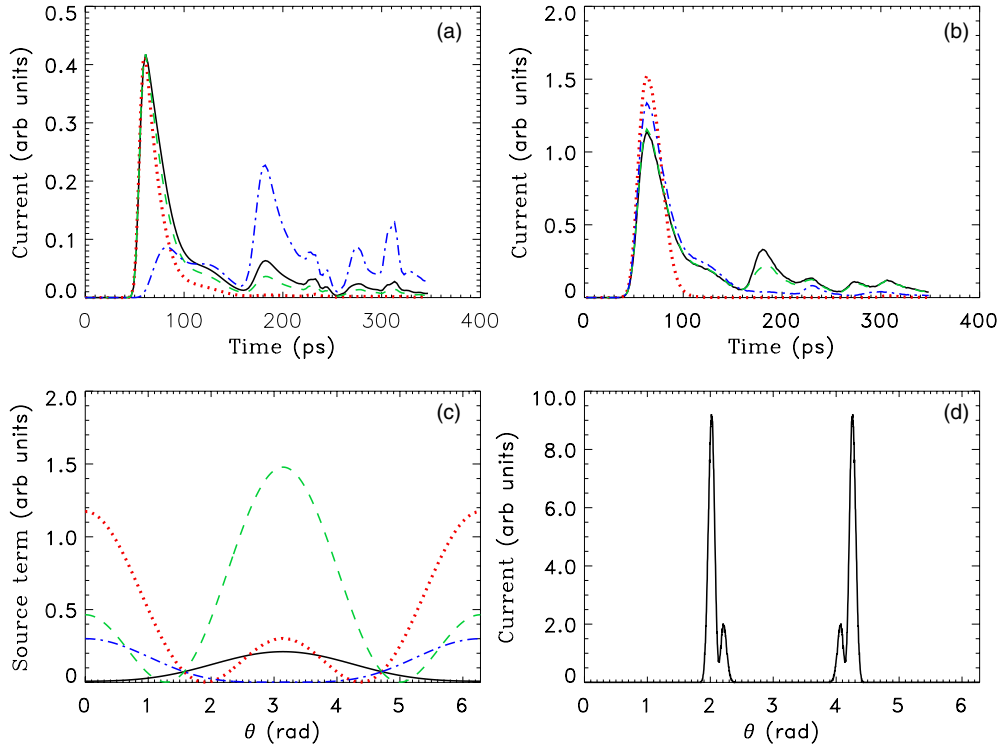
Figure 6. (a) Current–time plots from quantum-mechanical wave packet calculations for various angular distributions of the source term. All the angular distributions we tried have at most a single node in the angular range $[0, \pi]$ and are plotted as a function of θ in (c). Black solid curve has no nodes whereas blue dash-dotted curve has node at $\theta = \pi$ rad, green dashed curve at $\theta = 1.28$ rad, and the read dotted curve at $\theta = 1.9$ rad. Part (b) shows ionization current from the CTMC calculations for various exclusions from the angular range of the launch angle shown in (d). Black solid curve allows this entire range whereas red dotted curve completely excludes it from its allowed launch angles. Blue dash-dotted and green dashed curves are obtained by excluding the angular ranges $[1.8, 2.123]$ rad and $[1.998, 2.035]$ rad from the distribution shown in (d).

Superposing higher angular momentum components can help make the node sharper. Such a wave packet may be experimentally tailored by first exciting a ground state hydrogen to a low-n state in an external electric field. The fact that the electric field mixes states with $l \pm 1$ gives rise to Stark oscillations in the l-distribution. This forms a Stark wave packet, which then can be excited to a Rydberg wave packet via a second laser pulse. Hitting this Stark wave packet at the right time would enable one to control the l-distribution of the initial wave packet at the time of its launch to the Rydberg wave packet. For instance, exciting the ground state up to a wave packet within the $n = 2$ manifold results in a wave packet composed of $l = 0, 1$ and 2 angular momentum components, mixed in a time-dependent fashion. Hitting this wave packet with the second laser pulse at the right moment would launch it with a desired superposition of $l = 0, 1$ and 2 states to a high-n Rydberg wave packet. Since the Stark period would be longer compared to the period of the laser pulse, with the proper timing of the second laser pulse, a desired nodal pattern can be achieved for the initial wave packet.

To eliminate the second pulse in figure 1(c), we have excluded the launch angles in the range $[1.8, 2.4]$ rad in our CTMC calculation and placed a node at $\theta = 1.9$ rad in the angular

distribution of the source term in the quantum-mechanical wave packet calculation. The results are the red dotted curves in figures 6(a) and (b) for quantum and classical calculations, respectively. Clearly excluding the entire range of angles that make up the peaks in figure 6(d) does not only remove the second pulse in figure 1(c), but knocks out the entire pulse train after the direct ionization pulse. This means that the excluded angular range does not only give rise to the electrons that escape through the second pulse of electrons but also includes almost all the other trajectories that escape afterwards within the time range we explore. This is in accord with the previous classical calculations of Mitchell *et al* [17, 18] since the angular range we excluded is actually larger than the entire range they explored and resolved for particular peaks in the pulse train. The fact that the direct pulse remains intact in this case is expected since it is mainly risen by the trajectories that are launched directly downhill, i.e. $\theta = \pi$.

Instead of removing the entire angular range that makes up the peak in figure 6(d), we tried to remove smaller ranges of the classical launch angle θ within this peak. Results of these classical calculations can be summarized by the set of curves in figure 6(b).

(a) Allowing the full $[0, 2\pi]$ range for the launch angles in the classical calculations gives the solid black curve in figure 6(b). This is the case investigated previously.

(b) Excluding a thin slice from the centre of the angular distribution depicted in figure 6(d), i.e. the range [1.998, 2.035] rad, gives the green dashed curve of figure 6(b). In this case, the second peak has gotten smaller and the rest of the pulse train remains intact.

(c) Excluding a large slice of launch angles from the peak in figure 6(d) such that only the small secondary peak is left gives the blue dash-dotted curve of figure 6(b). Note that the second peak has now completely disappeared along with the later pulses in the pulse train except a large fraction of the third pulse. Comparing with the case in which the entire peaks in figure 6(d) were excluded (red dotted curve), this suggests that the small secondary peaks in the launch angular distribution is almost entirely responsible for the third pulse in the pulse train.

To simulate the same effect in our quantum calculations, we placed nodes at various angles in the angular distribution of the source term, i.e. the initial wave packet. Figure 6(c) shows several angular distributions we have tried and the resulting current–time plots make up figure 6(a). The same line-styled and coloured curves in figures 6(a) and (c) correspond to each other.

(a) The black solid curve in figure 6(a) corresponds to the angular distribution depicted by the black solid curve in figure 6(c) with no nodes and a maximum at $\theta = \pi$ rad. This angular distribution reproduces the current–time curve in figure 1(c) almost exactly.

(b) The blue dash-dotted curve in figure 6(a) has an angular distribution with a node at $\theta = \pi$ rad as seen in figure 6(c). This knocks out the direct pulse in figure 1(c) as expected since this is classically equivalent to removing the first prominent escape segment in figure 2(b).

(c) The green dashed curve of figure 6(a) is calculated using an angular distribution with a node at $\theta = 1.28$ rad which corresponds to the angular distribution in figure 6(c) with the same line style. Note that the direct pulse in this case remains unchanged while the second pulse is clearly reduced. This is because the node is not placed exactly at the centre of the main classical peak in figure 6(d) but it is close enough such that it partially knocks it out.

(d) When we place a node at $\theta = 1.9$ rad, at the centre of the classical peak in figure 6(d), we get the red dotted curve in figure 6(a). This kills off the entire pulse train following the direct pulse as in the classical case shown with the red dotted curve in figure 6(b).

Classically this is the same as killing off the escape segments labelled as **A1** and **A2** in figure 2(b).

To sum up, we find that we can diminish the pulse train as much as we want by sliding the node within the classically calculated peaks of figure 6(d). We were also able to remove the direct ionization pulse by placing a node at π. This is physically identical to killing off the trajectories that were classically launched directly downhill. Elimination of the pulses by inserting nodes in the angular distribution of the quantum-mechanical initial wave packet would be more clear and isolated from the neighbouring pulses if the corresponding classical escape segments in figure 2(b) were to span wider angular ranges.

3.5. Effect of core scattering

We have already pointed out that in the presence of a pure electric field, the hydrogen atom ionizes only via a direct pulse due to the absence of a core. In the presence of a core, the direct ionization peak is followed by an irregular train of ionizing electrons due to the part of the wavefunction which did not directly ionize but initially headed uphill, turned around by the uphill potential and then scattered in all directions by the core electrons [25]. Non-hydrogenic atoms in external electric fields have also been found to show statistical properties in the nearest-neighbour spacings that are neither regular nor chaotic suggesting that the dynamics is somewhere in between [26]. Therefore introducing a core into our problem may reveal interesting features attributable to the coupling between these two different dynamics.

We incorporated the core electrons into our calculations through a model potential. Instead of modelling a real atom using a model potential with proper quantum defects, it is more informative to use a model potential of the form $Ce^{-r/a}/r$. Playing with the parameters C and a we can control the range of the core potential. This allows us to control the extent of the core penetration by the electron.

Figures 7(c) and (d) show potentials for $C = -1$ and two different values of a along with the field-free potential of the hydrogen atom for $l = 0, 1$ and 2. The values used for a are 0.05 and 0.5 for figures 7(c) and (d), respectively. The model potentials are plotted as the black solid curves whereas the field-free hydrogenic potentials are the red dotted, blue dashed, and black dash-dotted lines for $l = 0, 1$, and 2, respectively. Note that in case of $a = 0.05$ the model core potential is buried deep below the angular momentum barrier even for the lowest angular momentum considered, i.e. $l = 0$. It is natural to expect the core potential to have no effect on the ionization dynamics in which we are interested, and this is indeed the case. The fully quantal ionization pulse train for this case is the black solid curve in figure 7(a). The same case within our CTMC model is again the black solid curve in figure 7(b). Both classical and fully quantal computations yield exactly what was seen for hydrogen in figure 1 due to the inability of the electron to penetrate into the core region. Increasing a to 0.5 we extend the range of the core potential beyond the $l = 1$ potential barrier and obtain red-dotted curves in figures 7(a) and (b) using quantum-mechanical and CTMC methods respectively. Figure 7(a) also shows the pure electric field case for $a = 0.5$ (blue dashed curve). Contrasting the black solid curve with the red-dotted curve in figure 7(a) we can tell that the addition of the core potential that extends beyond the $l = 1$ potential barrier enhances the pulses that come after the second pulse in the train with an additional pulse of electrons dwelling on the skirt of the second pulse (marked as P). This new pulse is absent in the classical calculation in figure 7(a) suggesting that it is due to interference between the parts of the wavefunction that scatters from the core and the part that is escaping due to chaotic nature of the time-dependent dynamics.
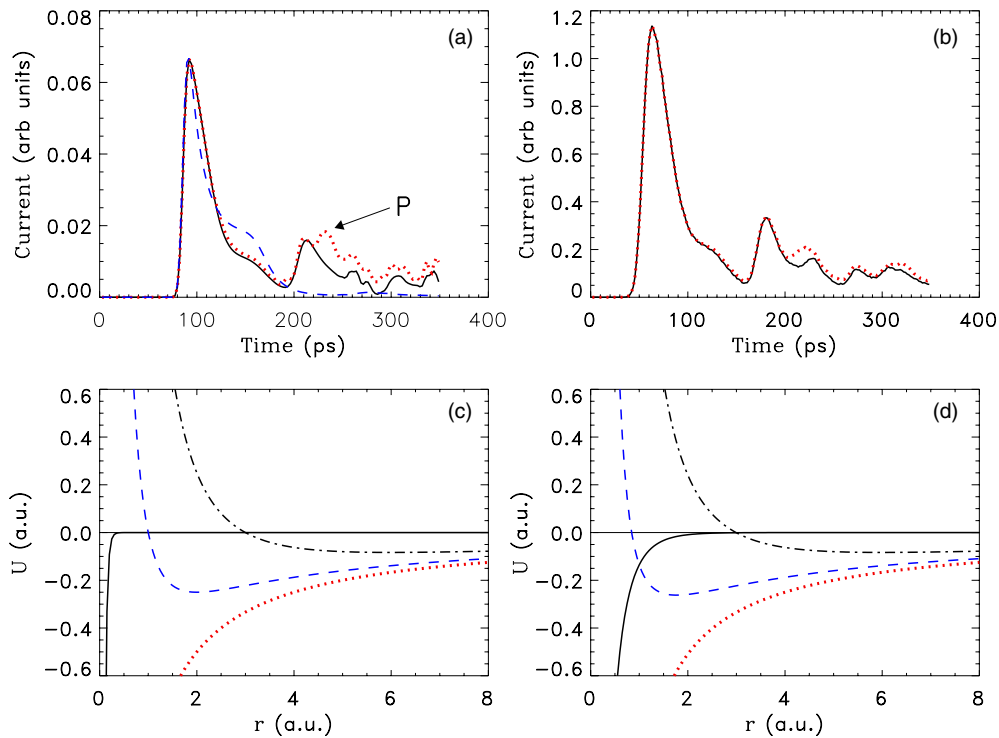
Figure 7. Quantum-mechanical (a) and classical (b) current–time plots with the inclusion of core scattering. In (a) the black solid curve is for $C = -1$ and $a = 0.05$ and the red dotted curve is for $C = -1$ and $a = 0.5$. The blue dashed curve shows the pure electric field case in the absence of chaos. In (b) again the black solid curve is for $C = -1$ and $a = 0.05$ and the red dotted curve is for $C = -1$ and $a = 0.5$. The difference is less prominent compared to the quantum-mechanical case in (a). Parts (c) and (d) show the model core potentials curves (black solid lines) and the field-free atomic potential curves for $l = 0$, 1, and 2 for $a = 0.05$ and $a = 0.5$, respectively. All the calculations are for $n = 80$.

3.6. Transition to regularity—the case of high magnetic fields

Transition from regular to chaotic dynamics in open atomic systems has been extensively studied in the energy domain for the diamagnetic Kepler problem and ionization of Rydberg atoms in external microwave fields. In the latter system, as the microwave frequency is varied from low to high, the dynamics pass through three distinct dynamical regimes of ionization. With the definition of a scaled frequency $\Omega_0 = \Omega n^3$ (the ratio of the microwave frequency Ω to the Kepler frequency of the Rydberg state $1/n^3$), microwave ionization in these regimes is categorized as the tunnelling, chaotic and the multiphoton ionization regimes. In the diamagnetic Kepler problem, introduction of a scaled parameter $\eta = E/\gamma$ transforms this problem into a problem of two coupled two-dimensional harmonic oscillators where the coupling strength is quantified by η. By changing η, or equivalently changing magnetic field strength γ for fixed energy E, transition from regularity to chaos is observed by studying the statistical distributions of the nearest-neighbour energy level spacings [27].

Due to the scaling properties of the classical Hamiltonian of the diamagnetic Kepler problem, the dynamics of the electron does not depend on the energy of the electron and the magnetic field independently, but rather depends on a scaled energy $E_c = E/\gamma^{2/3}$ [28].
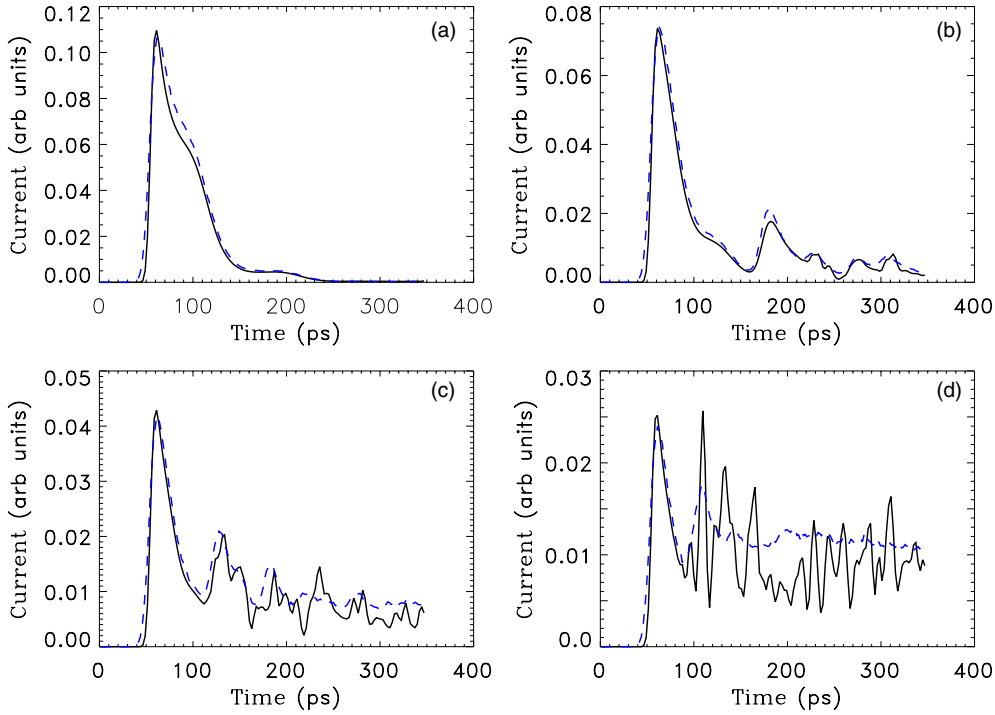
Figure 8. Quantum-mechanical (black solid curves) and classical (blue dashed curves) current–time plots for four different scaled energies quantified by α: (a) $\alpha = 0.5$, (b) $\alpha = 1.0$, (c) $\alpha = 2.0$ and (d) $\alpha = 4.0$. All the calculations are for $n = 80$.

Several properties of the diamagnetic Kepler problem have been studied by fixing the scaled energy E_c such as the quasi-Landau modulations in the photoabsorption spectra of diamagnetic hydrogen. So far in our study of the ionization of diamagnetic hydrogen in uniform electric field, we have only considered a single ionization regime and observed signatures of chaos in the current, wavefunctions and angular momentum distributions of the ionized electrons. This dynamical regime corresponds to $E_c \approx 0.48$ for all the energies and magnetic field strengths we have considered in previous sections.

We now will study different field regimes with different scaled energies while keeping the energy E and the electric field strength fixed. We particularly consider the $n = 80$ case and the scaled energies $E_c = \alpha^{-2/3}(E/\gamma^{2/3})$ with $\alpha = 0.5, 1.0, 2.0,$ and 4.0 where $\alpha = 1.0$ being the case we have studied in section 3.1. These scaled energies simply correspond to magnetic field strengths of $\alpha\gamma$, i.e. $B = 0.245$ T, $B = 0.49$ T, $B = 0.98$ T, $B = 1.96$ T respectively, and $E = 1/(2n^2) = 7.8 \times 10^{-5}$ (au) and $F = 19$ V cm^{-1}. The current–time plots we have obtained are plotted in figures 8(a)–(d) in increasing magnetic field strength, i.e., α. Each plot shows quantum-mechanical wave packet and CTMC results on top of each other for comparison. In the case of $\alpha = 0.5$ of figure 8(a), the time-dependent ionization dynamics appears regular. This is expected since for a weak enough magnetic field the dynamics is dominated by the external electric field and the magnetic field has little effect. The case of the pure electric field gives a single ionization pulse as discussed before leading to the prominent direct pulse in figure 8(a) with no further escape at later times. The regularity in this case is a direct consequence of the integrability of the system due to the separability of

the classical equations of motion and the agreement is perfect between the CTMC and the quantum-mechanical calculations. Figure 8(b) is the case for which $\alpha = 1.0$ which is what we have considered in section 3.1 and the ionization is chaotic with very good agreement between the classical and the quantum-mechanical current–time plots.

Figures 8(c) and (d) show the time-dependent current of ionizing electrons for $\alpha = 2.0$ and $\alpha = 4.0$. Note that the irregular structure of the ionization pulses from the CTMC calculation gets washed out compared to the $\alpha = 1.0$ case. This is expected since the higher the magnetic field, the closer we are to the Landau regime where the energy levels become similar to those of the harmonic oscillator. Therefore the diamagnetic Kepler problem in a uniform parallel electric field is integrable in this regime since a harmonic oscillator in uniform parallel electric field is integrable. The fact that the Landau regime is integrable leads to regularity in the classical dynamics in this regime as displayed by the dashed CTMC calculations in figures 8(c) and (d). Transition towards regularity displayed in the CTMC calculations can also be understood in the semiclassical grounds. The volume of a unit phase-space cell is proportional to the inverse of the effective Planck constant divided by 2π, i.e. $1/\hbar_{\text{eff}}$ which scales like $\sim 1/n$ [29]. Instead of increasing the magnetic field strength γ, we might just as well decrease n and maintain the same scaled energy E_c. This would simply increase the volume of the unit phase-space cell, giving rise to blurring and hence washing out of the fine structures in the phase space, suppressing chaos. In contrast to the classical case, the fully quantum-mechanical results show more erratic fluctuations relative to the $\alpha = 1.0$ case. This situation is even more pronounced for the case of $\alpha = 4.0$ in figure 8(d). Even though the structure of the pulse train in this case gives a strong impression of chaos, these enhanced oscillations in the quantum case do not necessarily point to enhanced chaos. Actually, given the fact that the CTMC calculations suggest transition to regularity in the underlying classical dynamics as α is increased, it can be concluded that the enhanced fluctuations in the quantum-mechanical current–time plot are not due to enhanced chaos but rather are results of a different physical mechanism.

The reason for the enhanced fluctuations for the higher magnetic fields can be understood if one considers how the number of open ionization channels change as the magnetic field is increased. Since we are closer to the Landau regime in the high-α (or magnetic field strength) limit, the energy levels become more like the Landau levels. In this case, the energy levels are almost equally spaced by ω_c as for a harmonic oscillator and the separation increases linearly with increasing magnetic field strength. For a fixed electric field strength, the classical ionization threshold is fixed at $-2\sqrt{F}$ and this gives a fixed opening for ionization since the azimuthal symmetry is the dominant symmetry in the system in the Landau regime. Any escaping trajectory must pass through this opening. For $n = 80$ at $F = 19 \text{V cm}^{-1}$, the energy is $E = -1/(2n^2) \approx -7.8 \times 10^{-5}$ (au) and the classical ionization threshold is $\mathcal{E} = -12.2 \times 10^{-5}$ (au). Therefore the size of the opening is $\Delta W = E - \mathcal{E} = 4.4 \times 10^{-5}$ (au). On the other hand, the Landau level spacing ω_c is 2.09×10^{-6} (au) and 4.18×10^{-6} (au) for $\alpha = 2.0$ and $\alpha = 4.0$, respectively. The ratio $\Delta W/\omega_c$ roughly gives the number of channels available for ionization and is ~ 21 for $\alpha = 2.0$ and ~ 10 for $\alpha = 4.0$. In the quantum-mechanical case, the number of ionization channels that fit into this opening therefore decrease with the increasing separation of the equally spaced energy levels. This is what gives rise to the enhanced oscillations in the quantum-mechanical current–time plot in figure 8(d).

One of the interesting phenomena observed for the diamagnetic Kepler problem is the quasi-Landau modulations in the photoabsorption spectrum at the zero-field threshold [30]. These modulations were originally observed to be separated by 1.5 times the Landau spacings for a free electron in magnetic field and are associated by the resonance states which are fairly localized in the plane perpendicular to the external magnetic field. Later wave packet
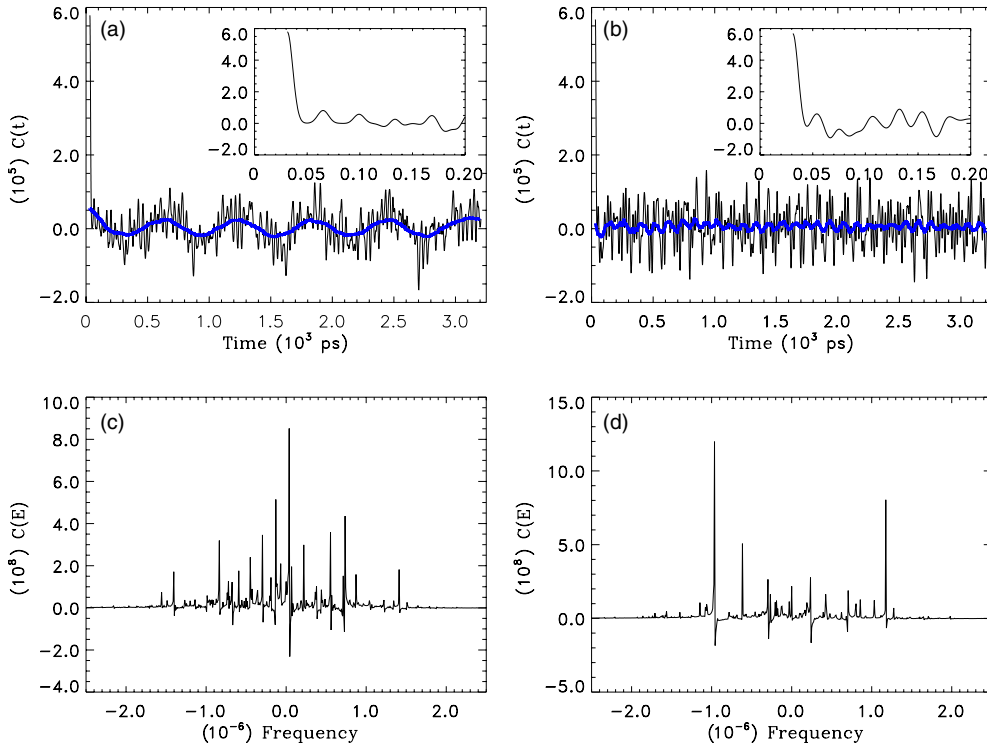
Figure 9. Time-dependent autocorrelation functions for (a) $\alpha = 1.0$ and (b) $\alpha = 4.0$. (c) and (d) are the spectral autocorrelation functions that correspond to (a) and (b) respectively. The time-dependent autocorrelation functions clearly show two types of oscillations whereas the spectral autocorrelation functions show equally spaced resonances which indicates Landau quantization.

calculations pointed out other Landau resonances with energy spacings of $0.64\omega_c$ [31]. Such quasi-Landau fluctuations were also seen at lower energies and explained in terms of the individual magnetic field states [32]. It was found that it was the highest energy diamagnetic states of the n-manifolds evolved into the Landau states [33]. To see whether such effects occur in our problem, we have evaluated the time-dependent autocorrelation function $C(t)$, and the corresponding spectral autocorrelation function $C(E)$ for the $\alpha = 2.0$ and $\alpha = 4.0$ cases of figure 8. The real part of $C(t)$ for each case is plotted as the black solid curves in figures 9(a) and (b), respectively. The blue solid curves are obtained from the autocorrelation functions by smoothing them via boxcar averaging. The insets in the figures show $C(t)$ near $t = 0$. Note in the $\alpha = 2.0$ case there are clearly two modes of oscillation in the autocorrelation function; the thick blue oscillation modulated by much narrower fluctuations in time. Both types of oscillations correspond to revivals of particular pieces of the wavefunction and manifest themselves in the spectral autocorrelation functions $C(E)$ in figures 9(c) and (d). The spectral autocorrelation function $C(E)$ in our case roughly corresponds to the photoabsorption spectrum. In the spectral autocorrelation functions, the frequency axis is shifted by $1/(2n^2)$ such that 0 frequency corresponds to the $n = 80$ component.

Both types of the oscillations depicted in figure 9(a) for $n = 80$ are due to the localized part of the wavefunction labelled as σ in figure 3(b), which is the Stark oscillating part of the wavefunction. In particular, the revival time of the sharper oscillations modulating the

oscillations depicted by the thick black curve in figure 9(a) is $t_{\text{rev}}^{(1)} \sim 40$ ps as can be seen from the inset. The revival time of the oscillation shown by the black thick curve for the same scaled energy is $t_{\text{rev}}^{(2)} \sim 600$ ps. These revival times correspond to energy spacings of $\Delta E_{\text{rev}}^{(1)} = 2\pi / t_{\text{rev}}^{(1)} \sim 3.8 \times 10^{-6}$ (au) and $\Delta E_{\text{rev}}^{(2)} = 2\pi / t_{\text{rev}}^{(2)} \sim 0.25 \times 10^{-6}$ (au). The spacings between the pronounced resonances of figure 9(c) have a spacing of $\sim 0.2 \times 10^{-6}$ (au) which roughly corresponds to $\Delta E_{\text{rev}}^{(2)}$. We do not see any resonances with spacings corresponding to $\Delta E_{\text{rev}}^{(1)}$ for this are almost as wide as the frequency range spanned by the resonances in figure 9(c). The spectral autocorrelation functions seen in figures 9(c) and (d) clearly show equally spaced resonances, much like the energy levels of a harmonic oscillator. This is due to the Landau quantization at the scaled energies we consider in figure 9. The number of such equally spaced resonances in figures 9(c) and (d) can be counted to be ~ 15 and ~ 8 respectively, which roughly agrees with the number of the ionization channels we have estimated above. The decrease in the number of Landau states is roughly a factor of 2 as would be expected, since the level spacing ω_c in the Landau regime linearly scales with the magnetic field strength, and the scaled energies considered in figures 9(a) and (c) and (b) and (d) are $\alpha = 2.0$ and $\alpha = 4.0$. Although we observe Landau states in the spectral autocorrelation function, we do not see any clear sign of quasi-Landau oscillations.

4. Conclusions

In this paper, we examined ionization of a hydrogen atom excited to a Rydberg state via a short laser pulse in parallel electric and magnetic fields. The field regime we have been interested in is that for which the classical dynamics of this system displayed chaos in the time domain as reported in [17, 18]. Since physical roots of irregular scattering are obscure and ill defined on purely quantum-mechanical grounds, we tried to explore the time-dependent dynamics of ionization from this system using a non-perturbative quantum-mechanical wave packet method along with a CTMC method.

Comparing quantum-mechanical and classical results from these calculations, we observed quantum-mechanical effects, which would be absent in the classical picture, such as interference effects. We have been able to reproduce chaos induced pulse trains of ionization, previously observed in classical calculations [17, 18]. We found very good agreement between our quantum-mechanical and classical calculations of the ionization current in the time domain for high Rydberg states with $n = 40, 60$ and 80. Looking at the time-dependent wavefunction of the system, we have observed flux of electrons that ionize through different pulses in the ionization pulse train and connected certain parts of the wavefunction with the classically observed escape segments in the classical time-dependent launch angle distribution of [18], which we have included in our paper as figure 2. We have found that as the ionization pulse train grows longer, the number of escape segments that contribute to a given pulse in the pulse train increases which ultimately leads to interference between different escape channels in the quantum-mechanical wavefunction. We have also observed these interference patterns on the surface of our spherical detector which confirmed the observation of previous classical calculations suggesting that the launch angle of a classical trajectory determines the time of the electron's escape, giving rise to a train of pulses in the time-dependent ionization current. Although the total ionization current, which is obtained by integrating the current density through the surface of the spherical detector, from the classical and the quantum-mechanical calculations, agrees very well, this does not mean that the classical and the quantum-mechanical pictures do not differ from one another. The main difference is the quantum interference discussed in section 3.3, whose effect on the current gets washed out when the current density is integrated through the surface of the detector. Another difference

between the classical and the quantum-mechanical pictures is that the classical picture lacks the phase information which is incorporated into the quantum calculations through the time propagation operator. A semi-classical modelling of this problem could shed light into the question of how important the phase information omitted is in the classical calculations.

This angular dependence of the shape suggested that it was possible to tailor the shape of the pulse train by using a proper angular distribution of the initial wave packet. In an attempt to manipulate the structure of the ionization pulse train, we ran CTMC simulations to figure out in which angular range a trajectory must be launched to contribute to the second pulse in the pulse train. Excluding this range of angles from the launch angular distribution in the CTMC calculations, we have eliminated pulses from our classical time-dependent ionization current. We further placed nodes at corresponding angles in the angular distribution of the initial wave packet in our quantum-mechanical wave packet calculations, and successfully removed the second and the prominent direct pulses from the pulse train.

We have also investigated the angular momentum distributions of the electrons inside the region bounded by our spherical detector. We were able to recognize the part of the l-distribution that corresponds to the direct ionization pulse which extended up to $l \sim 200$. This part of the distribution almost completely diminishes after the direct pulse terminates and the small fraction of the remaining decays away slowly since the prominent escape segment in the classical escape-time plot seen in figure 2(b) contributes to all the later pulses in the pulses train. We found that the angular momenta of the electrons escaping through the later pulses are confined to smaller l's than those escape through the direct pulse.

Inclusion of core scattering into our problem allowed us to study the extent to which the core penetration of the electron can affect the structure of the chaos-induced pulse train. We used a model core potential to allow $l = 0$ and $l = 1$ core penetrations of the electron. We reproduced our previous hydrogenic results for the $l = 0$ case as would be expected, and observed enhancements in the pulses that came after the second pulse in the pulse train for the $l = 1$ case. This enhancement of the pulses was more prominent in our quantum-mechanical simulations than in our CTMC simulations.

To study the transition from chaotic dynamics to regularity in this system, we varied scaled energy of the system and found that for high scaled energy, i.e., high magnetic field, the approach to the Landau regime resulted in the transition to regular regime in the classical dynamics implied by the suppression of chaotic structure of the ionization pulse train. On the other hand, our quantum-mechanical calculations showed enhanced oscillations in the current–time plot in this field regime. We have concluded that this was due to the decrease in the number of open ionization channels in the quantum case. Looking at the time-dependent autocorrelation function, we were able to see revivals of the Stark oscillating part of the time-dependent wavefunction and the resonances that correspond to them in the spectral autocorrelation function. We observed equally spaced resonances in the spectral autocorrelation function which we believe to be due to the Landau quantization in the strong magnetic field strengths we consider. Despite the apparent existence of the Landau quantization in the spectral autocorrelation function, we see no clear signatures of quasi-Landau oscillations.

Acknowledgments

References

[1] Blümel R and Reinhardt W P 1997 *Chaos in Atomic Physics* (Cambridge: Cambridge University Press)
[2] Heller E J 1984 *Phys. Rev. Lett.* **53** 1515
[3] Du M L and Delos J B 1988 *Phys. Rev.* A **38** 1896
[4] Main J, Wiebusch G, Welge K, Shaw J and Delos J B 1994 *Phys. Rev.* A **49** 847
[5] Freund S, Ubert R, Flöthmann E, Welge K, Wang D M and Delos J B 2002 *Phys. Rev.* A **65** 053408
[6] Brody T A, Flores J, French J B, Mello P A, Pandey A and Wong S S M 1981 *Rev. Mod. Phys.* **53** 385
[7] Berry M 1989 *Phys. Scr.* **40** 335
[8] Blümel R and Smilansky U 1988 *Phys. Rev. Lett.* **60** 477
[9] Ericson T 1960 *Phys. Rev. Lett.* **5** 430
[10] von Brentano P, Ernst J, Hausser O, Mayer-Kuckuk T, Richter A and von Witsch W 1964 *Phys. Rev. Lett.* **9** 48
[11] Ihra W, Mota-Furtado F and O'Mahony P F 1998 *Phys. Rev.* A **58** 3884
[12] Moser I, Mota-Furtado F and O'Mahony P F 1997 *Phys. Rev.* A **55** 3724
[13] Cacciani P, Luc-Koenig E, Pinard J, Thomas C and Liberman S 1988 *J. Phys. B: At. Mol. Opt. Phys.* **21** 3499
[14] Peters A D and Delos J B 1993 *Phys. Rev.* A **47** 3020
[15] Neumann C, Ubert R, Freund S, Flöthmann E, Sheehy B, Welge K, Haggerty M and Delos J B 1997 *Phys. Rev. Lett.* **78** 4705
[16] Jensen R V, Susskind S M and Sanders M M 1991 *Phys. Rep.* **201** 1
[17] Mitchell K A, Handley J P, Tighe B, Flower A and Delos J B 2004 *Phys. Rev. Lett.* **92** 073001
[18] Mitchell K A, Handley J P, Tighe B, Flower A and Delos J B 2004 *Phys. Rev.* A **70** 043407
[19] Topçu T and Robicheaux F 2006 *Phys. Rev.* A **73** 043405
[20] Kleiman U, Topçu T, Pindzola M S and Robicheaux F 2006 *J. Phys. B: At. Mol. Opt. Phys.* **39** L61
[21] Merzbacher E 1998 *Quantum Mechanics* 3rd edn (New York: Wiley)
[22] Topçu T, Pindzola M S, Ballance C, Griffin D C and Robicheaux F 2006 *Phys. Rev.* A **74**
[23] Press W H, Flannery B P, Teukolsky S A and Vetterling W T 1988 *Numerical Recepies in C* (New York: Cambridge University Press)
[24] Bethe H A and Salpeter E E 1957 *Quantum Mechanics of One- and Two-Electron Systems* (Berlin: Springer)
[25] Robicheaux F and Shaw J 1997 *Phys. Rev.* A **56** 278
[26] Jonckheere T, Gremaud B and Delande D 1998 *Phys. Rev. Lett.* **81** 2442
[27] Wintgen D and Friedrich H 1986 *Phys. Rev. Lett.* **57** 571
[28] Wintgen D and Friedrich H 1987 *Phys. Rev.* A **36** 131
[29] Benenti G, Casati G, Maspero G and Shepelyansky D L 2000 *Phys. Rev. Lett.* **84** 4088
[30] Gallagher T F 1994 *Rydberg Atoms (Cambridge Monographs)* (New York: Cambridge University Press)
[31] Holle A, Wiebusch G, Main J, Hager B, Rottke H and Welge K H 1986 *Phys. Rev. Lett.* **56** 2594
[32] Economou N P, Freeman R R and Liao P F 1978 *Phys. Rev.* A **18** 2506
[33] Gay J C, Delande D and Biraben F 1980 *J. Phys. B: At. Mol. Phys.* **13** L729